Contents list available at CBIORE journal website

International Journal of Renewable Energy Development

Journal homepage: https://ijred.cbiore.id

Research Article

Molecular simulation of single N and double N/S doping to carbon networks and the effect of doping dispersant

Arikasuci Fitonna Ridassepri[a,b,c], Fitria Rahmawati[a*], Agung Tri Wijayanta[d], Dedi Rohendi[e], Dyah Purwaningsih[f], Shota Sato[c], Jun Nakamura[c]

[a]*Research Group of Solid-State Chemistry & Catalysis, Chemistry Department, Faculty of Mathematics and Natural Sciences, Universitas Sebelas Maret, Jalan Ir. Sutami 36 A, Kentingan Surakarta 57126, Indonesia*

[b]*Chemistry Department, Mathematic and Natural Science Faculty, Universitas Negeri Surabaya, Surabaya, East Java, 60231, Indonesia*

[c]*Department of Engineering Science, University of Electro-Communications (UEC Tokyo), Tokyo, 182-8585, Japan*

[d]*Research Group of Sustainable Thermofluids, Mechanical Engineering, Sebelas Maret University, Jl. Ir. Sutami 36 A Kentingan, Surakarta, 57126, Indonesia*

[e]*Chemistry Department, Sriwijaya University, Jl. Masjid Al Gazali, Bukit Lama, Kec. Ilir Bar. I, Kota Palembang, Sumatera Selatan, 30128, Indonesia*

[f]*Chemistry Department, Universitas Negeri Yogyakarta, Jl. Colombo Yogyakarta No.1, Karang Malang, Caturtunggal, Kec. Depok, Kabupaten Sleman, Daerah Istimewa Yogyakarta 55281, Indonesia*

Abstract. This research conducted a molecular simulation of single N and double N/S doping into a carbon network. The simulation aimed to explain the effect of N and N/S doping, which was investigated experimentally by our previous research, and to prove the hypothesis that N and/or S replace a normal C site within the carbon crystal structure. Experimental data agree with the simulation result, as shown by the increasing ID/IG ratio in the Raman spectrum, which indicates defect formation after doping. Meanwhile, the XRD patterns of the doped carbon are similar to those of the undoped carbon. It suggests that the dopants N and/or S diffused and replaced the C atom from its normal site in the carbon crystal structure without forming new N and/or S-based compounds. The result is consistent with different dispersants investigated in this research, i.e., deionized water and ethanol. However, ethanol provided better dispersibility than water, resulting in a modified N/S carbon material with ethanol dispersant, NSCE, with a higher electrical conductivity of 23.74 x 10^{-1} Scm^{-1} than the N/S-modified carbon with water dispersion, NSCW, i.e., 5.97 x 10^{-1} Scm^{-1}. The presence of defects increases the number of sites for charge carriers to migrate within the carbon network, making it a good electrode material for an LFP battery, with an initial charging capacity of 349.94 ± 79.04 mAh/g and an initial discharge capacity of 113.41 ± 12.59 mAh/g. The results reveal N/S-doped carbon as a sustainable candidate for lithium-ion batteries and other advanced energy storage technologies.

Keywords: N-doped carbon, N/S-doped carbon, Molecular Simulation, Doping Dispersant.

Received: 22nd May 2025; Revised: 28th January 2026; Accepted: 16th June 2026; Available online: 13th July 2026

1. Introduction

Amorphous or hard carbon is well known as a promising anode material for secondary batteries, whether for Lithium-Ion Batteries (LIBs) or Sodium-Ion Batteries (SIBs), for its good chemical stability, high surface area, and good thermal stability (Chairunnisa *et al.*, 2021; Tang *et al.*, 2017; Wang, Hu, *et al.*, 2019; Xiong *et al.*, 2018). The partial-graphitic structure of hard carbon can accommodate Li^+/ Na^+ ions either between layers, interlayers, or within carbon pores (Duan *et al.*, 2020; Khosravi *et al.*, 2014; Xiong *et al.*, 2018). Our previous research found that a double N/S doping to carbon produced from bagasse, a solid waste of sugarcane production, shows good electrode performance for a sodium-ion battery by delivering initial charge-discharge capacity of 720 $mAhg^{-1}$ and 570 $mAhg^{-1}$, respectively, at 0.07 Ag^{-1}, with capacity retention of 57% after 50 cycles (Rahmawati *et al.*, 2024).

Some researchers have employed elemental doping of carbon networks or compositing with metal oxide to enhance the electrochemical properties of the carbon. Some elements, such as N, S, B, and P, have been doped into carbon (Y. Li *et al.*, 2016; Munir *et al.*, 2023; Qie *et al.*, 2012; Rahmawati *et al.*, 2011, 2014; Ridassepri *et al.*, 2024). The dopant is estimated to replace C atoms within a carbon unit cell, producing crystal defects due to the difference in oxidation numbers between the C atom and the dopant (Cheng *et al.*, 2019; X. Wu *et al.*, 2019; Xiong *et al.*, 2018). The replacement alters the electron distribution within the C crystal network due to changes in valence electrons and the formation of vacant sites.

Our previous research on double-doping N/S into a carbon structure produced from bagasse, a solid waste of sugar production, was conducted using thiourea as a dopant precursor and ethanol as a solvent (Rahmawati *et al.*, 2023; Ridassepri *et al.*, 2024). The research found an increase in defect formation

* Corresponding author
Email: fitria@mipa.uns.ac.id (F. Rahmawati)

https://doi.org/10.61435/ijred.2026.61404
ISSN: 2252-4940/© 2026.The Author(s). Published by CBIORE

due to N/S doping, as confirmed by the rise in the Raman ID-to-IG ratio from 0.92 to 1.15, indicating defect formation due to C replacement by the dopants N/S. However, it is hard to understand the doping mechanism from single N and S doping because simultaneous double N/S doping was used. Therefore, to address this critical knowledge gap, the current research further investigated the effects of single-N and double-N/S doping. Urea was used as a single N precursor, whereas thiourea was a double N/S precursor. To understand the possibility of water as a doping dispersant instead of ethanol, which is less environmentally considerate, this research also experimented by using both water and ethanol dispersants and compared the results. It is known that water and ethanol exhibit different dispersion properties due to their polarities. Ethanol is less polar than water, with respective dipole moments of 1.69 D and 1.85 D (Romero-Anaya *et al.*, 2015). The dispersion capabilities influence doping mechanisms and the properties of the resulting material, an aspect that previous studies have not explored, underscoring the novelty of this work.

Molecular simulations have been conducted to elucidate the atomic-level mechanisms of N and N/S doping in C networks, including predicting optimized structural configurations and mapping electrostatic potentials (ESP). Computational calculations provide detailed insights into dopant incorporation patterns and electronic-structure modifications, clarifying mechanisms that extend beyond the scope of prior empirical studies. Nitrogen doping occurs primarily through carbon substitution, forming graphitic N, pyridine N, and pyrrolic N. N-pyridine and N-pyrrolic donate electrons into the π-conjugate system of carbon, providing active sites and defects for additional reservoirs of lithium (Li^+) or sodium (Na^+) ions, as each can adsorb up to two Na^+ or Li^+ ions (Cheng *et al.*, 2019; Romero-Anaya *et al.*, 2015; X. Wu *et al.*, 2019). On the other hand, S doping, due to its larger atomic radius (102 pm) than carbon (77 pm), increases carbon interlayer spacing, generating additional active sites and facilitating Na^+ or Li^+ ion diffusion (Cheng *et al.*, 2019; Rahmawati *et al.*, 2024). As a result, the N/S heteroatom doping is expected to produce a synergistic effect, significantly enhancing electronegativity, interlayer spacing, and overall electrochemical performance of carbon materials.

Finally, a practical test was conducted on optimized carbon materials, based on theoretical predictions and experimental results, to investigate the visibility of the prepared N/S Carbon derived from the solid waste of sugarcane production. In summary, the current study employs a comprehensive approach, bridging theoretical molecular simulation and experimental synthesis to differentiate the effects of single- and double-N/S doping, evaluates water as an environmentally friendly dispersant, and provides novel structural predictions, significantly advancing the understanding and development of doped carbon materials for energy storage applications.

2. Experimental

2.1 Preparation of Carbon and Its Activation

Bagasse, a byproduct of sugarcane production, was procured from a sugarcane industry in Kudus, a city in central Java Province, Indonesia. The bagasse was immersed in deionized water for 24 hours, and then the water was removed. The remaining wet bagasse was dried in an oven at 120°C for 24 hours. The dry-cleaned bagasse was then carbonized at 600°C for 30 min under N_2 gas flow. The carbonized char was then activated in a furnace at 700 °C for 1 hour under steam flow. The detailed scheme of the activation reactor can be checked in our previous (Ridassepri *et al.*, 2020). The activation result was then analyzed using X-ray diffraction (Rigaku Miniflex 600), FTIR (Shimadzu IR Prestige-2), SEM/EDX (JEOL JSM-6510 LA), and surface area analysis (Quantachrome Instruments Nova 1200e).

Table 1
Sample names based on the dopant and the solvent used.

Sample	Dopant	Solvent used for doping
AC (Activated-carbon)	-	-
NCW	N	Distilled-water
NCE	N	Ethanol
NSCW	N/S	Distilled-water
NSCE	N/S	Ethanol

2.2 Nitrogen and Nitrogen/Sulfur Co-doping into Hard Carbon

The hard carbon was ground into a homogeneous powder with a 100-mesh size. The powder was then mixed with urea (p.a., Merck) for N doping and with thiourea (p.a., Merck) for N/S co-doping, using a mass ratio in grams (g) of 1:1 carbon-to-dopant precursor ratio for each. 30 mL of ethanol or distilled water was added to the mixture, followed by 2 hours of stirring at room temperature to obtain a homogeneous carbon dispersion. The dispersion was then heated in an oven at 80 °C for 6 h. The result was a solid deposit at the bottom of the flask. The deposit was isolated and then calcined at 850°C for 2 hours with a temperature ramp of 24.9 °C/min. The calcination was conducted under an N_2 gas flow at a rate of 20 mL/min. The powder was then cooled at room temperature and was ready for analysis. Each product was named based on the dopant and the solvent used for doping. Details are provided in Table 1. The schematic illustration of the doping process in this research is based on simulation calculations using the Gaussian16 package (Frisch *et al.*, 2016). All the resulting products were analyzed and compared with the undoped carbon.

2.3 Impedance Analysis

The prepared carbon was mixed with acetylene black (AB;

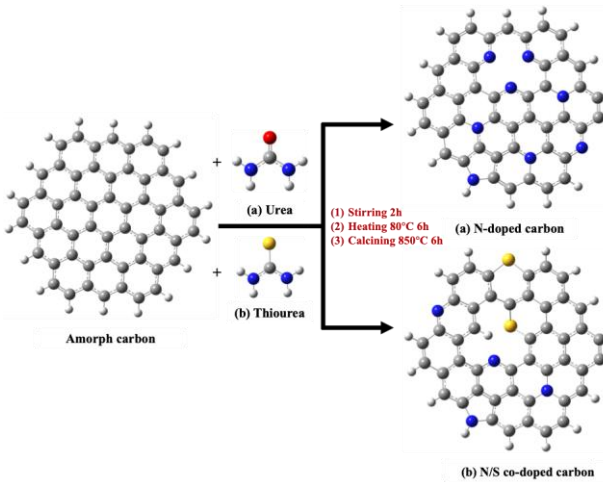

Fig.1 Schematic illustration of the single N or N/S co-doped carbon in this research. Activated carbon is mixed with urea or thiourea using 30 mL of methanol or distilled water as solvents, followed by stirring (2 hours), heating at 80°C (6 hours), and calcination at 850°C (6 hours) under N_2 gas flow.

KGC Saintifik Indonesia) and ground in an agate mortar until homogeneous. The mixture was then dried in an oven (Memmert UN30-1060 E7086) at 60°C for 45 min. Another step was to dissolve PVDF (KGC Saintifik Indonesia) in N-Methyl-2-Pyrrolidone (NMP) (KGC Saintifik Indonesia) by gradually adding the NMP dispersant while stirring. The AB and carbon mixture was gradually poured into the PVDF/NMP solution under stirring conditions, and the slurry was stirred for 4 h to ensure homogeneity and remove air. The AB:PVDF:NMP ratio was 7:2:1, according to another research (Xiong *et al.*, 2018). The carbon slurry was then cast onto Cu foil using the tape-casting method and dried in a vacuum oven (B-One Vacuum Oven VOV-50, 220V/1400W) at 80 °C for 12 h. For comparison, a similar preparation was also conducted with commercial mesocarbon microbeads, MCMB. All electrode films were then prepared for impedance measurements.

The carbon/Cu film was cut by an electrode cutter. Two silver wires were connected to the carbon/Cu film using silver paste, and the film was then dried in an oven at 70°C for 30 minutes. The area of the silver paste should be accurately measured as the area of the active electrode (A, cm^2), and the distance between the silver wire should also be calculated as *l* (cm). The detailed scheme of the prepared sample for impedance measurement is depicted in Figure 2. Impedance analysis was conducted over the frequency range of 20 Hz – 500 kHz (LCR meter, EUCOL, 20 Hz – 5 MHz).

2.4 Battery Fabrication and Measurement

The NSCE powder was used as anode material by mixing 94.5 wt% of NSCE powder with acetylene black (1 wt%), carboxymethyl cellulose (2.25 wt%), and styrene-butadiene rubber (2.25 wt%), which were used as binders. At the same time, deionized water functioned as the solvent. The mixture was then stirred until a homogenous slurry was obtained. A doctor blade cast the homogeneous paste on Cu foil (MSK-AFA II). The anode thickness was 100 µm and heated at 120 °C for 24 h (Natalia *et al.*, 2019). Meanwhile, the LFP slurry was formulated by blending 90.2 wt% LFP powder with PVDF (3.7 wt%), acetylene black (1.5 wt%), KS-6 (4.6 wt%), and N-methyl-2-pyrrolidone (NMP) solvent. The mixture was stirred until homogeneous, cast on Aluminum foil at 250 µm, and dried at 120°C overnight in a vacuum oven. The battery was assembled in a cylinder case within an Ar glove box. The electrolyte composition consisted of 1 M $LiPF_6$ in EC/DMC, with a polypropylene membrane serving as the separator (Natalia et al., 2019).

2.5 Simulation Works

All quantum mechanical computations were conducted using the Gaussian16 package (Frisch *et al.*, 2016), employing first-principles approaches grounded in Density Functional Theory (DFT). The pristine graphene layer consists of 54 C atoms and 18 H atoms ($C_{54}H_{18}$). The model is a finite cell containing an edge-passivated C atom bound to an H atom. All models were computed utilizing Becke's three-parameter hybrid method approach in combination with Lee-Yang–Parr exchange-correlation energy functional (B3LYP) (Stephens *et al.*, 1994) in combination with the 6-31G(d,p) basis set with gas phase, employing open boundary conditions. This model used the Restricted Kohn-Sham (RKS) theory for calculations and employed spin pairing for closed-shell singlets, yielding zero spin contamination. Vibrational frequency calculations were performed to confirm the absence of imaginary frequencies across all models.

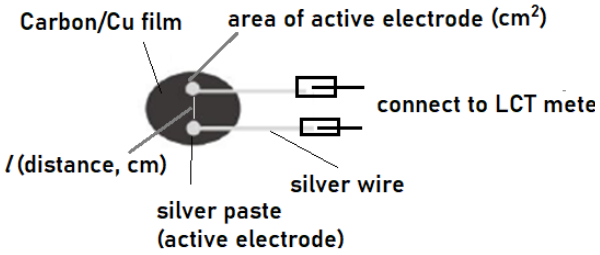

Fig. 2. Scheme of the prepared sample for impedance measurement.

3. Result and Discussion

XRD analysis was conducted on the steam-activated carbon and the doped carbons. All prepared carbon shows a similar characteristic peak, as depicted in Figure 3. The peaks lie broadly at approximately 2θ = 25° and 2θ = 44°, which correspond to the (002) and (100) planes of graphitic carbon, as referenced in the standard diffraction data for graphitic carbon, JCPDS #41-1487, and supported by previous studies (Elkholy *et al.*, 2023; Shahcheragh *et al.*, 2023; Shi *et al.*, 2016). The broad peaks indicate the amorphousness of the prepared carbon (Wang, Hu, *et al.*, 2019).

Raman analysis was also conducted on all prepared carbons to assess the effects of N and N/S doping on the activated carbon. All prepared carbon shows two broad peaks at 1350 and 1590 cm^{-1} (Figure 4). Those two broad peaks are in line with other research on hard carbon, which defines the peaks as D and G bands(Xiong *et al.*, 2018). The D band is revealed by structural distortion induced by N and N/S doping. The N or N/S doping resulted in vacant sites as predicted by Kröger-Vink notation in equations (1) and (2),

$$C_6 + 4N \rightarrow C_C + 4N_C^{'} + V_C^{\bullet\bullet\bullet\bullet} \quad (1)$$

$$C_6 + 2N + S \rightarrow 2C_C + 2N_C^{'} + S_C^{''} + V_C^{\bullet\bullet\bullet\bullet} \quad (2)$$

in which the • sign refers to a negative charge relative to the initial, and the • sign refers to a positive charge relative to the previous condition. C replacement by N and C would change

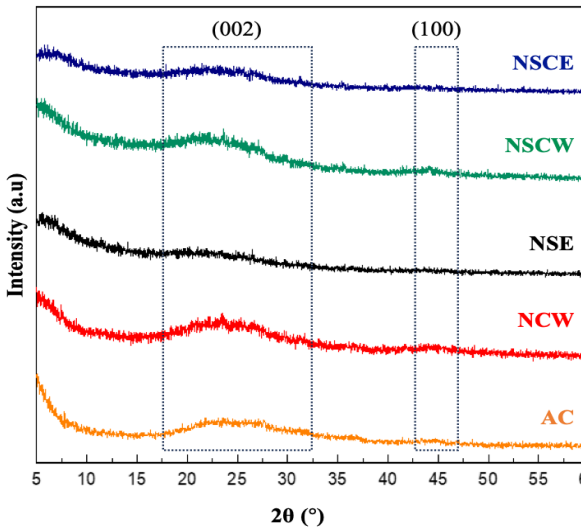

Fig.3 XRD patterns of the prepared carbon.

Table 2
I_D to I_G ratio of the prepared carbon.

Sample	Ratio of I_D/I_G
Activated-carbon	0.91
NCW	1.07
NCE	1.10
NSCW	1.12
NSCE	1.16

the electron distribution within the C crystal structure, and vacancy formation (VC••••) would increase charge transport, whether of ions or electrons. Meanwhile, the G band refers to the C atom under sp^2 hybridization, which indicates the presence of graphitic carbon within the prepared material (Wan & Hu, 2019). The ratio of D intensity, I_D, to G intensity, I_G, is used to determine the defect within the carbon structure. The I_D/I_G ratio of each prepared carbon is listed in Table 2.

Table 2 shows that doping to carbon increases I_D/I_G, representing the increase in structure distortion due to defect formation. N/S co-doping shows a higher I_D/I_G value, indicating more structure distortion due to 2 N atoms and one S atom could produce carbon vacancy, $V_C^{••••}$ (Eq.2). Meanwhile, 4 single N dopants were required to produce $V_C^{••••}$ (Eq.1). A higher value of I_D/I_G also indicates that the produced carbon is more amorphous (Wang *et al.*, 2019). The atomic size of S is 102 pm, much larger than the sizes of N and C, which are 75 pm and 77 pm, respectively (Yuan *et al.*, 2020). Therefore, C substitution with S increased the interlayer distance between carbon networks, thereby izZZmproving electrode performance. For example, suppose the prepared carbon is used in a LIB or SIB. In that case, it will enable Li^+ or Na^+ ions in the battery electrolyte to intercalate and deintercalate between carbon layers during battery charging and discharging. It will increase the electrochemical activity and capacitive storage of the device (Wan & Hu, 2019; Wang, Hu, *et al.*, 2019; Xiong *et al.*, 2018).

FTIR analysis of the prepared carbon () reveals O-H vibration at 3446 cm^{-1}, C-H vibration at 2884 cm^{-1}, C=C vibration at 1570 cm^{-1}, and C-O vibration at 1092 cm^{-1}. The N-doped-C and N/S-doped-C spectra show a broad vibrational band around 3400 cm-1, corresponding to the C-OH vibration. The broad peak of the O-H vibration ensures the polarity and

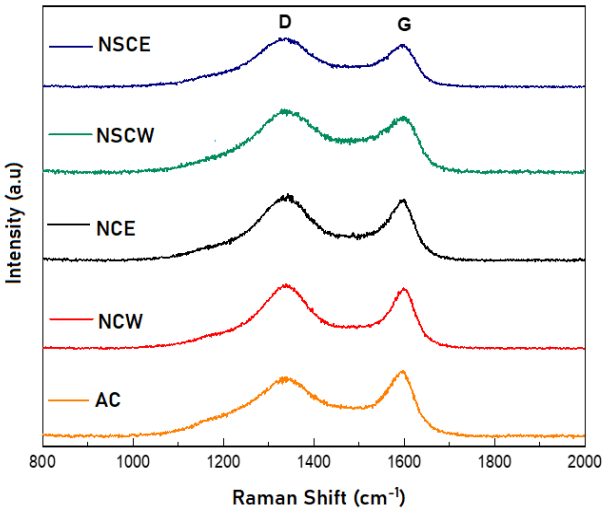

Fig. 4 Raman spectrum of the prepared carbon.

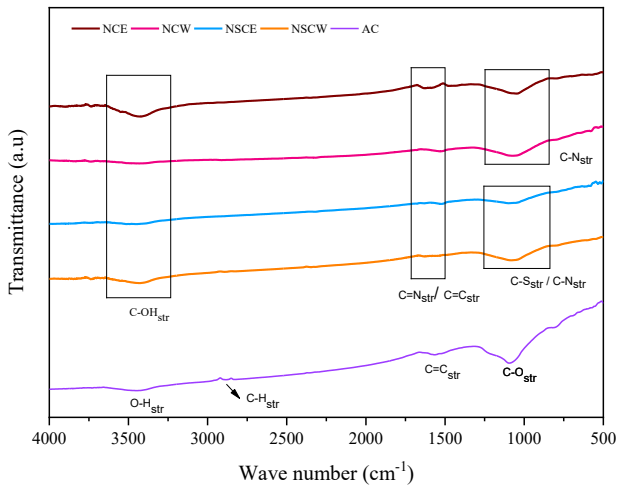

Fig. 5 FTIR spectra of the prepared carbon

high hydrophilicity of the doped carbon (Luo *et al.*, 2018). A vibration at 1048 cm^{-1} for NCE and 1066 cm^{-1} for NCW indicates the presence of C-N stretching (Xu *et al.*, 2014). Meanwhile, N/S doped-carbon, whether NSCW or NSCE, shows vibration at 1083 cm^{-1} and 1084 cm^{-1}, respectively, according to the presence of C-N stretching and/or C-S stretching (Luo *et al.*, 2018; Rochman *et al.*, 2019). The vibration at 1500 cm^{-1} belongs to C=N stretching and C=C stretching (D. Li *et al.*, 2026; Rochman *et al.*, 2019). The presence of C=N and C-N vibration indicates the bonding formation of C with the N dopant. Meanwhile, C-S vibration refers to the formation of a C-S bond.

Surface morphology images, as described in Fig. 6. The prepared carbon exhibits an irregular form. Furthermore, EDS analysis informs the presence of C and O within N-doped carbon and the presence of C, O, and S within the N/S doped-carbon. EDS mapping result can be seen in Fig. 6. Light element detection, such as $N_{K\alpha}$ can be decreased significantly due to the presence of carbon because carbon has a high mass absorption coefficient at around 25500 cm^2g^{-1} to the X-ray line. In addition, the X-ray detector window experiences decreased transmission at deficient X-ray line energy (Liao, 2006).

The EDS map (Fig. 6) shows an even distribution of the S element on the carbon surface, with a higher S content in doped carbon prepared from an ethanol solution (1.61 %) than in that prepared from a distilled water solution (0.88 %). Naturally, sulfur is not soluble in water but is slightly soluble in ethanol (Mokhatab *et al.*, 2015; Steudel, 2020). Therefore, ethanol could disperse S in carbon better than water.

An XPS analysis of the NSCE from previous results (Rahmawati et al., 2024) provided a detailed discussion of the chemical bonding detected in the doped materials, further confirming the structural modifications caused by N/S doping. The combination of XPS and Raman analyses underscores the significant role of heteroatom doping in increasing structural defects and enhancing electronic properties.

Surface area analysis of the prepared carbon shows the isotherm of adsorption-desorption, as depicted in Fig. 7. All the prepared-carbon type A isotherms indicate micro- and mesoporous materials (Yanbin et al., 2008). BET surface area, as listed in Table 3, shows that carbon prepared using ethanol has a higher surface area than that prepared using distilled water. The pore size of all prepared carbon lies between 1.89 – 1.90 nm (7(b)), suggesting that defects in the carbon structure

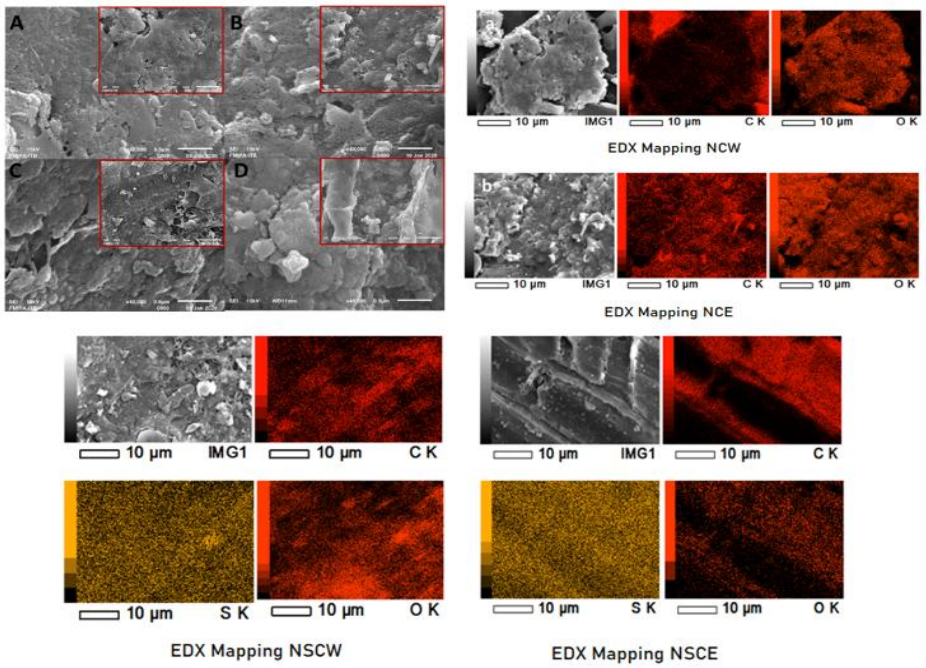

Fig. 6 Surface morphology or SEM Images of (a) NCW, (b) NCE, (c) NSCW, (b) NSCE and EDX mapping of NCW, NCE, NSCW, and NSCE.

Table 3
Surface area of the prepared carbons.

Materials	BET Specific Surface Area (m^2/g)	Total Pore's Volume (cc/g)	Average Pore Size (nm)
Steam activated-carbon	396.41	0.33	1.672
NCW	123.61	0.04	1.897
NCE	405.83	0.20	1.901
NSCA	174.85	0.06	1.892
NSCE	337.86	0.11	1.903

caused by N or N/S doping contribute to homogenizing the pore size of the carbons.

However, doped carbon prepared using an ethanol solvent exhibits a higher pore volume than that prepared with distilled water, and is higher than steam-activated carbon. This indicates that ethanol contributes to pore formation, resulting in deeper pores and a higher specific surface area. The activated carbon exhibits a higher total pore volume than N-doped carbon despite having a smaller specific surface area, indicating the presence of larger mesopores or macropores in the activated carbon, which dominate the pore volume contribution. In contrast, N-doped carbon shows a higher BET surface area, likely due to a higher proportion of smaller mesopores or micropores, which provide more surface area but contribute

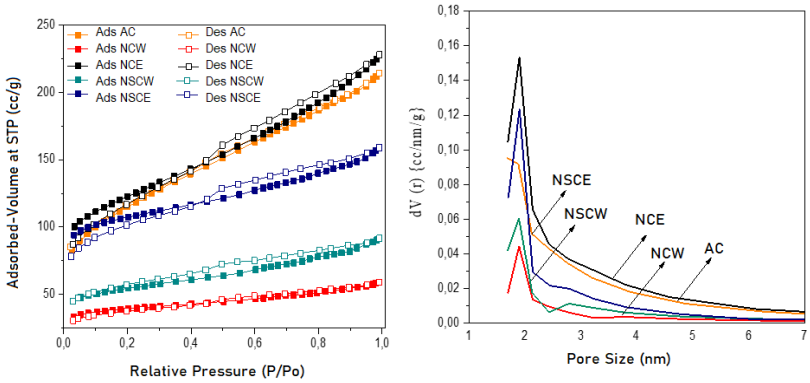

Fig. 7 Adsorption isotherm of the prepared carbon and pore distribution of the prepared carbon.

Table 4
Electric resistance and electric conductivity of the prepared carbon.

Materials	Resistance (Ω)		Conductivity (S/cm)	
	f = 20 Hz	f = 200 kHz	f = 20 Hz	f = 200 kHz
Activated-carbon	42.80	33.84	2.42×10^{-1}	3.06×10^{-1}
Commercial-mcmb	25.60	25.56	3.50×10^{-1}	3.50×10^{-1}
NCW	14.17	14.22	5.40×10^{-1}	5.38×10^{-1}
NCE	13.53	13.56	5.43×10^{-1}	5.41×10^{-1}
NSCA	6.98	7.00	5.98×10^{-1}	5.97×10^{-1}
NSCE	4.49	4.50	23.74×10^{-1}	23.70×10^{-1}

less to the total pore volume, as illustrated in Fig. . The combination of uniform pores, high pore volume, and high surface area supported the material's performance as an electrode. These characteristics allow the high-surface-area material to accommodate Li+ or Na+ ions during the charge-discharge process (Duan *et al*., 2020; Hernández-rentero *et al*., 2020; Ma *et al*., 2018; Xiong *et al*., 2018).

Impedance analysis was conducted to investigate the electrical conductivity of each prepared carbon. The measurement was performed over 20 Hz–500 kHz, considering the electronic conduction properties of carbon, which typically dominate impedance responses at low frequencies. The plot of resistance to the applied frequency is described in Fig. 8. Meanwhile, resistance values at 20 Hz and 200 kHz are listed in Table 4 Along with electric conductivity σ (Scm^{-1}), values that were calculated by equation (3),

$$\sigma = \frac{1}{R}\frac{l}{A} \qquad (3)$$

In which R is resistance (Ω), l is the distance between two active electrodes (cm), and A is the active area of the electrode (cm^2). The R values were measured at low frequencies (20 Hz) and at 200 kHz.

The result (Fig. 8) shows that single N- and N/S co-doping into carbon significantly decreases the resistance from 42.80 to 4.49 at 20 Hz after N/S doping with ethanol as the solvent. The resistance drop was more pronounced when N/S co-doping

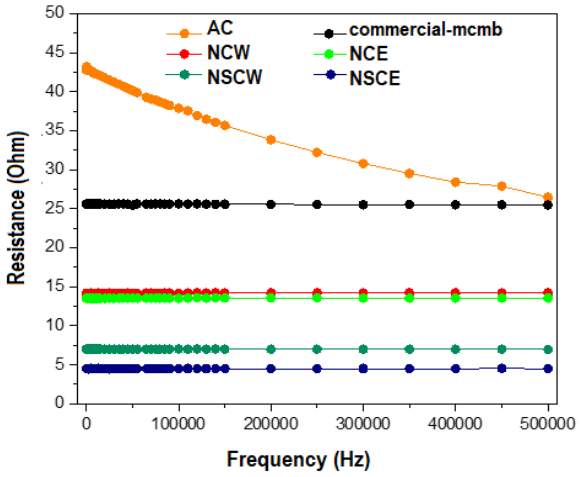

Fig. 8 Resistance at various frequency measurement of the prepared-carbon compared to the commercial-mcmb.

was performed in ethanol than in distilled water. Furthermore, N/S co-doping yields a larger decrease in resistance than single N doping. Reducing resistance improves conductivity, with ethanol providing higher carbon conductivity than distilled water. Carbon doped under ethanol solvent exhibits superior physicochemical properties as an electrode compared to carbon doped under water. This is attributed to the improved dispersion of hard carbon in ethanol, as shown in Fig. 9, which facilitates a more optimal doping process by increasing the interfacial area between carbon and the N dopant precursors (urea) and the N/S dopant precursor (thiourea). Carbon powder disperses better in ethanol, as shown by Fig.9(b), than in water, because ethanol is moderately polar with a dipole moment of ~1.69 Debye (Book, 2023). which is lower than the water dipole moment, ~1.89 Debye (Zhu & Voorhis, 2021), which is categorized as highly polar. Meanwhile, solid carbon is a nonpolar molecule that would interact less with highly polar molecules than with moderately polar molecules.

Table 4 also shows that N/S co-doping yields a higher electrical conductivity of carbon than single N doping. This can be attributed to the higher electronegativity of N (3.04) and S (2.58) compared to C (2.55), which increases the negative charge density within the carbon network (Liu *et al*., 2018). As a result, resistance decreased (Fig. 8) while conductivity improved (Table 4). The conductivity of N/S-doped carbon even surpasses that of commercial MCMB, demonstrating the strong potential of steam-activated carbon derived from sugarcane waste as a raw material for electrode fabrication.

Theoretical calculations were employed to investigate the impact of single N and N/S co-doping into the carbon structure. The optimized structures of pristine graphene, single N-doped carbon, and N/S co-doped carbon are illustrated in Fig. 10. All structures show no imaginary frequency, suggesting that all models proposed in this research are stable. The models of

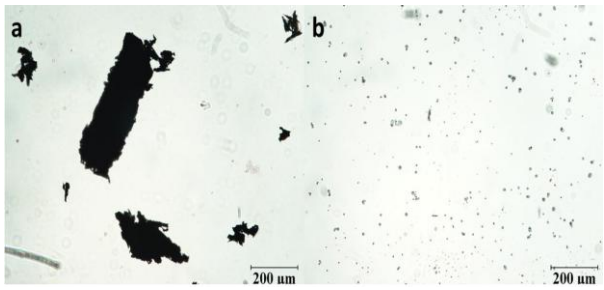

Fig. 9 Digital microscope images showing the interaction between hard carbon and different solvents: (a) deionized water and (b) ethanol.

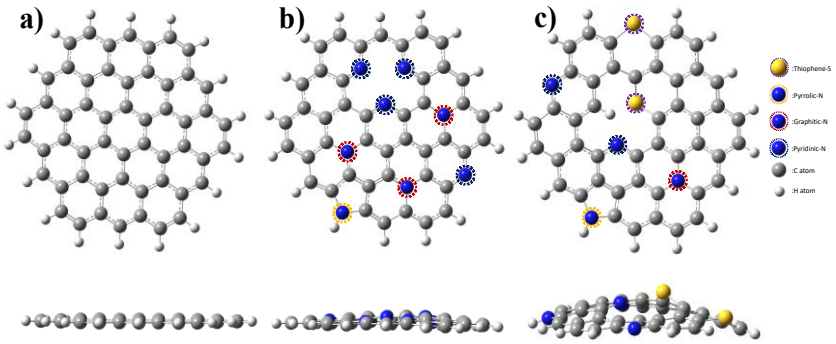

Fig. 10 Molecular structure top (upper) and side views (bottom) of (a) pure graphene, (b) single N-doped carbon, and N/S co-doped carbon.

single-N-doped carbon and N/S co-doped carbon were examined and compared with pristine graphene. The carbon structure in this study is considered to consist of graphene layers. The pristine graphene model (undoped) used in this study consists of 54 carbon (C) atoms and 18 hydrogen (H) atoms, i.e., $C_{54}H_{18}$, as shown in Fig. 10(a). Each carbon atom forms a bond with a hydrogen atom.

According to the Kröger-Vink notation, the doping mechanisms can be described by the reactions in Equations (1) and (2). In the N-doped carbon model, replacing a C atom with an N atom introduces N substitutional defects (N_C') and creates vacancies (V_C••••) in the lattice. The substitution of 8 N atoms results in 2 C atom vacancies. The single N-doped carbon model includes structures with pyridinic-N, pyrrolic-N, and graphitic-N doping configurations (Liu *et al.*, 2018), as displayed in Fig. 10(b). Meanwhile, in the N/S-doped carbon model, the substitution of 2 S atoms and 4 N atoms results in both N (N_C') and S (S_C'') substitutional defects, along with 2 C vacancies (V_C••••). The N/S-doped carbon structure comprises pyridinic-N, pyrrolic-N, graphitic-N, and thiophene-S configurations (Fig. 10(c)) (Liu *et al.*, 2018). Even though this study used a finite $C_{54}H_{18}$ cluster for simulation, the result shows similar defect formation and the position of N and S as expected by stoichiometric solid-state reaction defined in equations (1) and (2), and similar to our previous result on XPS analysis of N/S doped-C. The presence of pyrrolic-N as observed at 402.4 eV peak, and thiophene-S at 171.95 eV was proven by XPS analysis (Rahmawati *et al.*, 2024), which aligns with the electrochemical properties of the NSCE electrode, because the defect provided a negative charge area, as shown by Fig.11, that interacts strongly with Li^+ as an active ion in a lithium-ion battery.

According to the side views of all models in Fig. 10, doping carbon with N atoms induces minor distortions in the carbon structure, resulting in a slight surface curvature. Meanwhile, N/S co-doping leads to greater structural distortion, significantly increasing surface curvature. The N/S co-doped carbon exhibits more defects and irregularities in the carbon lattice, consistent with the Raman results in Fig. . These defects provide additional active sites that facilitate the intercalation of mobile ions within the carbon network, leading to increased conductivity and enhanced electrochemical reactions during the charge-discharge process.

Fig. 11 compares the electrostatic potential profile of pristine graphene, N-doped carbon, and N/S-doped carbon, providing significant insights into the charge distribution within the carbon structure. The electrostatic potential of pristine graphene is relatively uniform, indicating a balanced charge distribution across the C atoms with mostly green-yellow surface, suggesting a slightly negative charge distribution. Fig 11 shows that N doping results in a red area around 4 N atoms that replaced C, which is defined as N_C' by equation (1), bearing a negative charge because the 5 valence electrons of the N atom have replaced the 4 valence electrons of the C atom. As compensation, a defect C lattice was created at the edge as a blue area in the electrostatic potential surface (Fig 11(b)) representing the positive charge of the vacancy defect, $V_C^{\bullet\bullet\bullet\bullet}$, as a result of one 4-valence-electron C leaving the atom. The simulation result (Fig. 11(b)) clearly confirms the stoichiometric solid-state reaction given by equation (1). The nucleophilic behavior of N_C' serves as an active site for the Li^+/Na^+ intercalation-deintercalation process (Berenjaghi *et al.*, 2021; Sood *et al.*, 2018), because the negative charge of pyridinic-N possesses the capability of adsorbing two Li^+/Na^+ ions (Yuan *et al.*, 2020; Zheng *et al.*, 2014).

In the N/S-doped carbon models (Fig 11(c)), the thiophene-S dopant (the yellow dot) that replaces a 4 valence C atom results in S_C'' as predicted by equation (2), bearing a negative charge as confirmed by the red area. Meanwhile, N dopant has

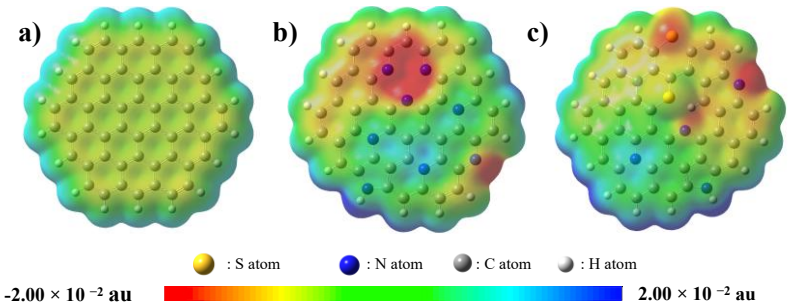

Fig. 11 Electrostatic potential surface at an isovalue of 0.001 au of (a) pristine graphene, (b) single N-doped carbon, and (c) N/S co-doped carbon. Red indicates negative values (-2.00 x 10^{-2} au), while blue indicates positive values (+2.00 x 10^{-2} au).

Table 5
Coulombic efficiency and specific charge/discharge capacities of the NSCE over five cycles.

Cycle-	Specific Charge Capacity (mAh/g)	Specific Discharge Capacity (mAh/g)	Coloumbic Efficiency (%)
1	349.94 ± 79.04	113.41 ± 12.59	32.14
2	122.83 ± 40.01	105.05 ± 22.31	85.52
3	110.04 ± 24.38	97.15 ± 17.63	88.28
4	103.65 ± 15.21	92.69 ± 11.58	89.43
5	95.79 ± 12.52	86.89 ± 10.41	90.70

replaced the C atom, resulting in two N_C' that bears a negative charge, as confirmed by the red area around the two blue dots (Fig. 11(c)). The negative surface charge resulting in simultaneous N/S doping required compensation to maintain the neutral charge of the whole pristine structure by removing a C atom, resulting in a vacancy $V_C^{\bullet\bullet\bullet\bullet}$ bearing a negative surface charge, as shown by the blue area at the edge of the pristine graphene (Fig 11(c)). The negative charge regions created by pyridinic-N and thiophene-S doping enhance the electrode materials' ability to interact with Li+/Na+ ions, facilitating their intercalation during charge-discharge cycles.

The charge-discharge evaluation was conducted as a feasibility study to investigate the potential of NSCE as a lithium-ion battery electrode. A LIB was then prepared with an NSCE anode and a $LiFePO_4$ cathode. Fig. 12 shows the charge-discharge analysis over five cycles at a current density of 15.89 mA/g. Table 5 found that the battery provides initial charging and discharging capacities of 349±79.04 mAh/g and 113.41±12.59 mAh/g, respectively, with a Coulombic efficiency of 32.14%. The low Coulombic efficiency of NSCE at the first cycle is attributed to the formation of a Solid Electrolyte Interphase (SEI) on its electrode surface. The SEI layer is formed due to the decomposition of the electrolyte and the irreversible reaction between the surface functional group and Li ions (Tang *et al*., 2017; J. Wu *et al*., 2021; Xiong *et al*., 2018; Zhao *et al*., 2020; Zhou *et al*., 2022), which is common in high-surface-area carbon material (Tang *et al*., 2017). The issue of low first-cycle Coulombic efficiency (%) due to the irreversible capacity loss can be overcome by several strategies, such as optimizing the binder (Su *et al*., 2024) or pre-lithiation (Han et al., 2024).

The Coulombic efficiency increases steadily across subsequent cycles, from 32.14% in the first cycle to 85.52%, 88.28%, 89.43%, and 90.70% in the fifth cycle, demonstrating electrode stabilization. The consistent increase in Coulombic efficiency highlights NSCE's ability to stabilize after initial side reactions. It suggests the potential of the N/S-doped carbon derived from sugarcane waste factories. However, further optimization is required to enhance its performance for practical applications.

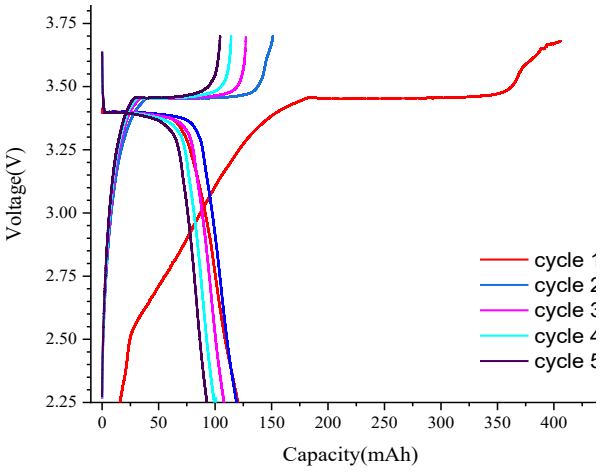

Fig. 12 Charge-discharge curve of NSCE-$LiPF_6$-LFP battery.

The electrochemical activity of the NSCE was compared to that of commercial activated carbon and biomass-derived carbon, as reported in previous studies. For instance, commercial activated carbon provides a specific capacity of approximately 50 mAh/g (Ahmed *et al*., 2023), while activated carbon sourced from olive pomace biomass delivers a 56 mAh/g capacity at a current density of 25 mA/g (Alouiz *et al*., 2025). In contrast, this study's N/S-doped carbon derived from bagasse waste material demonstrates a significantly higher specific capacity of 113.41±12.19 mAh/g at 15.89 mA/g at the first discharge. This improvement is attributed to the enhanced conductivity and structural modifications introduced by N/S doping, which optimize the carbon framework for Li-ion storage. The enhancement of electrochemical properties is attributed to the negatively charged region formed after doping (Fig. 11(b) and (c)), which increases interactions between the electrode material and Li^+ ions. Even though the simulation was conducted on a finite pristine graphene layer as a model, the simulation result is in agreement with our previous study in XPS analysis to a bulk sample NSCE (Rahmawati *et al*., 2024). The findings highlight the potential of N/S-doped carbons derived from sugarcane waste as superior alternatives to conventional activated carbons in energy storage applications. Beyond LIB applications, the N/S-doped carbon materials show potential for other energy storage systems. For instance, in supercapacitors, the high surface area and heteroatom doping could enhance charge storage by improving ion adsorption at the electrode interface.

4. Conclusion

Steam-activated carbon prepared from sugarcane waste holds significant potential as a sustainable raw material for electrode preparation. N and N/S co-doping were successfully achieved, as evidenced by the increasing ID/IG ratio in the Raman spectrum, indicating defect formation within the C crystal structure. The existence of C-N, C-S, and C=N vibrations in FTIR spectra further confirms successful doping. N and N/S co-doping effectively reduces the resistance of the materials, with N/S co-doping yielding a more pronounced decrease, thereby enhancing electronic conductivity. The electronic conductivity is even higher than the commercial, and the result increases significantly from 2.42 x 10^{-1} Scm^{-1} before doping to 23.74 x 10^{-1} Scm^{-1} after N/S doping. Simulation shows a synergistic effect of N and S atoms as dopants that promotes the

electrochemical process. A lithium battery with LFP and NSCE as electrodes also performs well, delivering an initial discharge capacity of 113.41±12.59 mAh/g. The N/S-doped carbon has a higher specific capacity than the commercial activated carbon from the previous study. The N/S-doped carbon appears to be a promising, sustainable candidate for advanced energy storage applications.

Acknowledgments

Universitas Sebelas Maret funded this research partly under the scheme of Penelitian Kolaborasi Perguruan Tinggi Dalam Negeri (PKPTDN) contract No. 2277.1/UN27.22/PT.01.03/2022.

Author Contributions: Arikasuci F Ridassepri: investigation, data curation, writing the original draft. Fitria Rahmawati: supervision, funding acquisition, writing, review, and editing. Agung T Wijayanta: supervision and review. Dedi Rohendi: material characterization and data analysis. Dyah Purwaningsih: data analysis and validation. Shota Sato: XPS analysis and data validation. Jun Nakamura: supervision, molecular model, and validation.

Funding: This research was funded by Penelitian Kolaborasi Perguruan Tinggi Dalam Negeri (PKPTDN) contract No. 2277.1/UN27.22/PT.01.03/2022.

Conflicts of Interest: The authors declare no conflict of interest.

References

Ahmed, F., Almutairi, G., Hasan, P. M. Z., Rehman, S., Kumar, S., Shaalan, N. M., Aljaafari, A., Alshoaibi, A., AlOtaibi, B., & Khan, K. (2023). Fabrication of a biomass-derived activated carbon-based anode for high-performance Li-Ion batteries. *Micromachines,* 14(1), 192 ; https://doi.org/10.3390/mi14010192

Alouiz, I., Aqil, M., Dahbi, M., Amarouch, M. Y., & Mazouzi, D. (2024). Performance of high-energy storage activated carbon derived from olive pomace biomass as an anode material for sustainable lithium-ion batteries. *Resources Chemicals and Materials*, 4(2), 100086; https://doi.org/10.1016/j.recm.2024.11.001

Berenjaghi, H. M., Mansouri, S., & Beheshtian, J. (2021). A DFT study on the potential application of pristine, B and N doped carbon nanocones in potassium-ion batteries. *Journal of Molecular Modeling,* 27(6), 168. https://doi.org/10.1007/s00894-021-04790-5

Book, C. (2023). *Overview of ethanol polarity*. https://www.chemicalbook.com/article/overview-of-ethanol-polarity.htm. Accessed on 5 June 2026.

Chairunnisa, Miksik, F., Miyazaki, T., Thu, K., Miyawaki, J., Nakabayashi, K., Wijayanta, A. T., & Rahmawati, F. (2021). Development of biomass based-activated carbon for adsorption dehumidification. *Energy Reports,* 7, 5871-5884; https://doi.org/10.1016/j.egyr.2021.09.003

Cheng, D., Zhao, Y., An, T., Wang, X., Zhou, H., & Fan, T. (2019). 3D interconnected crumpled porous carbon sheets modified with high-level nitrogen doping for high performance lithium sulfur batteries. *Carbon, 154*, 58-66; https://doi.org/10.1016/j.carbon.2019.07.094

Duan, M., Zhu, F., Zhao, G., Hu, J., Zhang, H., Ren, G., Meng, Y., & Fan, Z. (2020). Nitrogen and sulfur co-doped mesoporous carbon derived from ionic liquid as high-performance anode material for sodium ion batteries. *Microporous and Mesoporous Materials,* 306, 110433; https://doi.org/10.1016/j.micromeso.2020.110433

Elkholy, A. S., Yahia, M. S., Elnwawy, M. A., Gomaa, H. A., & Elzaref, A. S. (2023). Synthesis of activated carbon composited with Egyptian black sand for enhanced adsorption performance toward methylene blue dye. *Scientific Reports,* 13(1), 4209; https://doi.org/10.1038/s41598-023-28556-6

Frisch, M. J., Trucks, G. W., Schlegel, H. B., Scuseria, G. E., Robb, M. A., Cheeseman, J. R., Scalmani, G., Barone, V., Petersson, G. A., Nakatsuji, H., Li, X., Caricato, M., Marenich, A. V., Bloino, J., Janesko, B. G., Gomperts, R., Mennucci, B., Hratchian, H. P., Ortiz, J. V., Izmaylov, A. F., Sonnenberg, J. L., Williams, Ding, F., Lipparini, F., Egidi, F., Goings, J., Peng, B., Petrone, A., Henderson, T., Ranasinghe, D., Zakrzewski, V. G., Gao, J., Rega, N., Zheng, G., Liang, W., Hada, M., Ehara, M., Toyota, K., Fukuda, R., Hasegawa, J., Ishida, M., Nakajima, T., Honda, Y., Kitao, O., Nakai, H., Vreven, T., Throssell, K., Montgomery Jr., J. A., Peralta, J. E., Ogliaro, F., Bearpark, M. J., Heyd, J. J., Brothers, E. N., Kudin, K. N., Staroverov, V. N., Keith, T. A., Kobayashi, R., Normand, J., Raghavachari, K., Rendell, A. P., Burant, J. C., Iyengar, S. S., Tomasi, J., Cossi, M., Millam, J. M., Klene, M., Adamo, C., Cammi, R., Ochterski, J. W., Martin, R. L., Morokuma, K., Farkas, O., Foresman, J. B., & Fox, D. J. (2016). Gaussian 16 Rev. C.01. Wallingford, CT.

Han, D., Xiang, S., Cunha, J., Xie, Y., Zhou, M., Hou, Z., & Yin, H. (2024). Pre-lithiated silicon/carbon nanosphere anode with enhanced cycling ability and coulombic efficiency for lithium-ion batteries. *Journal of Energy Storage,* 79, 110183; https://doi.org/10.1016/j.est.2023.110183

Hernández-Rentero, C., Marangon, V., Olivares-Marín, M., Gómez-Serrano, V., Caballero, Á., Morales, J., & Hassoun, J. (2020). Alternative lithium-ion battery using biomass-derived carbons as environmentally sustainable anode. *Journal of Colloid and Interface Science,* 573, 396-408; https://doi.org/10.1016/j.jcis.2020.03.092

Khosravi, M., Bashirpour, N., & Nematpour, F. (2014). Synthesis of hard carbon as anode material for lithium ion battery. *Advanced Materials Research,* 829, 922-926; https://doi.org/10.4028/www.scientific.net/AMR.829.922

Li, D., Zhang, L., Chen, H., Ding, L.-x., Wang, S., & Wang, H. (2015). Nitrogen-doped bamboo-like carbon nanotubes: promising anode materials for sodium-ion batteries. *Chemical Communications,* 51(89), 16045-16048; https://doi.org/10.1039/C5CC06266G

Li, Y., Wang, G., Wei, T., Fan, Z., & Yan, P. (2016). Nitrogen and sulfur co-doped porous carbon nanosheets derived from willow catkin for supercapacitors. *Nano Energy,* 19, 165-175; https://doi.org/10.1016/j.nanoen.2015.10.038

Liao, Y. (2006). *Practical Electron Microscopy and Database*. In (pp. 1412).

Liu, Y., Qiao, Y., Wei, G., Li, S., Lu, Z., Wang, X., & Lou, X. (2018). Sodium storage mechanism of N, S co-doped nanoporous carbon: Experimental design and theoretical evaluation. *Energy Storage Materials,* 11, 274-281; https://doi.org/10.1016/j.ensm.2017.09.003

Luo, X., Zhang, W., Han, Y., Chen, X., Zhu, L., Tang, W., Wang, J., Yue, T., & Li, Z. (2018). N,S co-doped carbon dots based fluorescent "on-off-on" sensor for determination of ascorbic acid in common fruits. *Food Chemistry,* 258, 214-221; https://doi.org/10.1016/j.foodchem.2018.03.032

Ma, Y., Guo, Q., Yang, M., Wang, Y., Chen, T., Chen, Q., Zhu, X., Xia, Q., Li, S., & Xia, H. (2018). Highly doped graphene with multi-dopants for high-capacity and ultrastable sodium-ion batteries. *Energy Storage Materials,* 13, 134-141; https://doi.org/10.1016/j.ensm.2018.01.005

Mokhatab, S., Poe, W. A., & Mak, J. Y. (2015). Chapter 9 - Sulfur Recovery and Handling. In S. Mokhatab, W. A. Poe, & J. Y. Mak (Eds.), *Handbook of Natural Gas Transmission and Processing (Third Edition)* (pp. 301-334). Boston: Gulf Professional Publishing.

Munir, M. A., Rahmawati, F., Jamal, J. A., Ibrahim, S., Said, M. M., & Ahmad, M. S. (2023). Inspecting histamine isolated from fish through a highly selective molecularly imprinted electrochemical sensor approach. *ACS Omega,* 8(14), 13352-13361; https://doi.org/10.1021/acsomega.3c00768

Natalia, V., Rahmawati, F., Wulandari, A., & Purwanto, A. (2019). Graphite/Li_2ZrO_3 anode for a $LiFePO_4$ battery. *Chemical Papers,* 73(3), 757-766; https://doi.org/10.1007/s11696-018-0626-0

Qie, L., Chen, W.-M., Wang, Z.-H., Shao, Q.-G., Li, X., Yuan, L.-X., Hu,

X.-L., Zhang, W.-X., & Huang, Y.-H. (2012). Nitrogen-doped porous carbon nanofiber webs as anodes for lithium ion batteries with a superhigh capacity and rate capability. *Advanced materials (Deerfield Beach, Fla.),* 24(15), 2047-2050; https:/doi.org/10.1002/adma.201104634

Rahmawati, F., Amalia, A. F., Ridassepri, A. F., Nakamura, J., & Lee, Y. (2024). A Functional N/S-doped Carbon Electrode from a Carbonized Bagasse Activated with Water Vapor. *Journal of Electrochemical Science and Technology,* 15(4), 466-475; https://doi.org/10.33961/jecst.2024.00017

Rahmawati, F., Triana, K., & and Hastuti, A. (2011). Photo- and electro-catalysis for solar disinfection of Escherichia coli-contaminated water using Ag–TiO2/graphite. *Toxicological & Environmental Chemistry,* 93(8), 1602-1612; https://doi.org/10.1080/02772248.2011.604322

Rahmawati, F., Heliani, K. R., Wijayanta, A. T., Zainul, R., Wijaya, K., Miyazaki, T., & Miyawaki, J. (2023). Alkaline leaching-carbon from sugarcane solid waste for screen-printed carbon electrode. *Chemical Papers,* 77(6), 3399-3411; https://doi.org/10.1007/s11696-023-02712-8

Rahmawati, F., Wahyuningsih, S., & Irianti, D. (2014). The Photocatalytic Activity of SiO_2 -TiO_2/Graphite and Its Composite with Silver and Silver Oxide. *Bulletin of Chemical Reaction Engineering & Catalysis*, 9(1), 45–52; https://doi.org/10.9767/bcrec.9.1.5374.45-52

Ridassepri, A., Rahmawati, F., Raras Heliani, K., Somad, C., Miyawaki, J., & Wijayanta, A. (2020). Activated carbon from bagasse and its application for water vapor adsorption. *Evergreen,* 7, 409-416; https://doi.org/10.5109/4068621

Ridassepri, A. F., Umejima, Y., & Nakamura, J. (2024). B-doped fullerene as a potential metal-free catalyst material for CO reduction reaction. *The Journal of Physical Chemistry C,* 128(23), 9513-9519; https://doi.org/10.1021/acs.jpcc.4c01468

Rochman, R. A., Wahyuningsih, S., Ramelan, A. H., & Hanif, Q. A. (2019). Preparation of nitrogen and sulphur Co-doped reduced graphene oxide (rGO-NS) using N and S heteroatom of thiourea. *IOP Conference Series: Materials Science and Engineering,* 509(1), 012119; https://doi.org/10.1088/1757-899X/509/1/012119

Romero-Anaya, A. J., Lillo-Ródenas, M. A., & Linares-Solano, A. (2015). Factors governing the adsorption of ethanol on spherical activated carbons. *Carbon,* 83, 240-249. https://doi.org/10.1016/j.carbon.2014.10.092

Shahcheragh, S. K., Bagheri Mohagheghi, M. M., & Shirpay, A. (2023). Effect of physical and chemical activation methods on the structure, optical absorbance, band gap and urbach energy of porous activated carbon. *SN Applied Sciences,* 5(12), 313; https://doi.org/10.1007/s42452-023-05559-6

Shi, K., Pang, X., & Zhitomirsky, I. (2016). Silver nanoparticle assembly on carbon nanotubes triggered by reductive surfactant coating. *Materials Letters,* 178, 128-131; https://doi.org/10.1016/j.matlet.2016.05.005

Sood, P., Kim, K. C., & Jang, S. S. (2018). Electrochemical properties of boron-doped fullerene derivatives for lithium-ion battery applications. *ChemPhysChem,* 19(6), 753-758; https://doi.org/10.1002/cphc.201701171

Stephens, P. J., Devlin, F. J., Chabalowski, C. F., & Frisch, M. J. (1994). Ab initio calculation of vibrational absorption and circular dichroism spectra using density functional force fields. *The Journal of Physical Chemistry,* 98(45), 11623-11627; https://doi.org/10.1021/j100096a001

Steudel, R. (2020). The Chemical Sulfur Cycle. In (pp. 11).

Su, C., Gao, X., Liu, K., Dai, Y., Dong, H., Liu, Y., Zhu, J., Zhang, Q., He, H., & He, G. (2024). From lab to market: a review of commercialization and advances for binders in lithium-, zinc-, sodium-ion batteries. *Nano Research Energy,* 3, 2790-8119; https://doi.org/10.26599/NRE.2023.9120094

Tang, H., Wang, M., Lu, T., & Pan, L. (2017). Porous carbon spheres as anode materials for sodium-ion batteries with high capacity and long cycling life. *Ceramics International,* 43(5), 4475-4482; https://doi.org/10.1016/j.ceramint.2016.12.098

Wan, H., & Hu, X. (2019). Nitrogen/sulfur co-doped disordered porous biocarbon as high performance anode materials of lithium/sodium ion batteries. *International Journal of Hydrogen Energy,* 44(39), 22250-22262; https://doi.org/10.1016/j.ijhydene.2019.06.107

Wang, L., Hu, L., Yang, W., Liang, D., Liu, L., Liang, S., Yang, C., Fang, Z., Dong, Q., & Deng, C. (2019). N/S-Co-doped porous carbon sheets derived from bagasse as high-performance anode materials for sodium-ion batteries. *Nanomaterials,* 9(9); https://doi.org/10.3390/nano9091203

Wang, L., Wei, Z., Mao, M., Wang, H., Li, Y., & Ma, J. (2019). Metal oxide/graphene composite anode materials for sodium-ion batteries. *Energy Storage Materials,* 16, 434-454; https://doi.org/10.1016/j.ensm.2018.06.027

Wu, J., Ihsan-Ul-Haq, M., Chen, Y., & Kim, J.-K. (2021). Understanding solid electrolyte interphases: Advanced characterization techniques and theoretical simulations. *Nano Energy,* 89, 106489; https://doi.org/10.1016/j.nanoen.2021.106489

Wu, X., Ding, B., Zhang, C., Li, B., & Fan, Z. (2019). Self-activation of nitrogen and sulfur dual-doping hierarchical porous carbons for asymmetric supercapacitors with high energy densities. *Carbon,* 153, 225-233; https://doi.org/10.1016/j.carbon.2019.07.020

Xiong, J., Pan, Q., Zheng, F., Xiong, X., Yang, C., Hu, D., & Huang, C. (2018). N/S Co-doped carbon derived from cotton as high performance anode materials for lithium ion batteries. *Frontiers in chemistry,* 6, 78; https://doi.org/10.3389/fchem.2018.00078

Xu, X., Yuan, T., Zhou, Y., Li, Y., Lu, J., Tian, X., Wang, D., & Wang, J. (2014). Facile synthesis of boron and nitrogen-doped graphene as efficient electrocatalyst for the oxygen reduction reaction in alkaline media. *International Journal of Hydrogen Energy,* 39(28), 16043-16052; https://doi.org/10.1016/j.ijhydene.2013.12.079

Yanbin, Y., Dameng, L., Dazhen, T., Wenhui, H., Shuheng, T., & Yao, C. (2008). A comprehensive model for evaluating coalbed methane reservoirs in China. *Acta Geologica Sinica - English Edition,* 82(6), 1253-1270; https://doi.org/10.1111/j.1755-6724.2008.tb00727.x

Yuan, Y., Chen, Z., Yu, H., Zhang, X., Liu, T., Xia, M., Zheng, R., Shui, M., & Shu, J. (2020). Heteroatom-doped carbon-based materials for lithium and sodium ion batteries. *Energy Storage Materials,* 32, 65-90; https://doi.org/10.1016/j.ensm.2020.07.027

Zhao, W., Wen, J., Zhao, Y., Wang, Z., Shi, Y., & Zhao, Y. (2020). Hierarchically porous carbon derived from biomass reed flowers as highly stable Li-Ion battery anode. *Nanomaterials,* 10(2); https://doi.org/10.3390/nano10020346

Zheng, F., Yang, Y., & Chen, Q. (2014). High lithium anodic performance of highly nitrogen-doped porous carbon prepared from a metal-organic framework. *Nature Communications,* 5(1), 5261; https://doi.org/10.1038/ncomms6261

Zhou, R., Tan, H., Gao, Y., Hou, Z., Du, X., & Zhang, B. (2022). Constructing resilient solid electrolyte interphases on carbon nanofiber film for advanced potassium metal anodes. *Carbon,* 186, 141-149; https://doi.org/10.1016/j.carbon.2021.10.023

Zhu, T., & Voorhis, T. Van. (2021). Understanding the dipole moment of liquid water from a self-attractive hartree decomposition. *The Journal of Physical Chemistry Letters*, 12(1), 6–13; https://doi.org/10.1021/acs.jpclett.0c03300